Eur. Phys. J. C 27, 427–432 (2003)
Digital Object Identifier (DOI) 10.1140/epjc/s2002-01124-0

THE EUROPEAN
PHYSICAL JOURNAL C

Delineating the polarized and unpolarized photon distributions of the nucleon in eN collisions

M. Glück, C. Pisano, E. Reya, I. Schienbein

Universität Dortmund, Institut für Physik, 44221 Dortmund, Germany

Received: 2 October 2002 / Revised version: 9 December 2002 /

Abstract. The production rates of lepton–photon and dimuon pairs at the HERA collider and the HERMES experiment are evaluated in the leading order equivalent photon approximation. It is shown that the production rates are sufficient to facilitate the extraction of the polarized and unpolarized equivalent photon distributions of the proton and neutron in the available kinematical regions. It is pointed out that these results indicate the possibility of additional, independent, tests concerning the unpolarized and polarized structure functions $F_{1,2}^N$ and $g_{1,2}^N$, respectively, of the nucleon.

1 Introduction

In a previous publication [1] we presented the polarized and unpolarized equivalent photon distributions $(\Delta)\gamma^N(y,Q^2)$ of the nucleon, $N=p,n$, consisting of two components,

$$(\Delta)\gamma^N(y,Q^2)=(\Delta)\gamma_{\mathrm{el}}^N(y,Q^2)+(\Delta)\gamma_{\mathrm{inel}}^N(y,Q^2), \quad (1.1)$$

where the elastic parts, $(\Delta)\gamma_{\mathrm{el}}^N$, are due to $N\to\gamma N$, while the inelastic parts, $(\Delta)\gamma_{\mathrm{inel}}^N$, derive from $N\to\gamma X$ with $X\neq N$. It turns out that, as in the case of $\gamma_{\mathrm{el}}^p(y,Q^2)$ studied in [2], $(\Delta)\gamma_{\mathrm{el}}^N(y,Q^2)$ are uniquely determined by the well-known electromagnetic form factors $F_{1,2}^N(q^2)$ of the nucleon. The inelastic components were fixed via the boundary conditions [1]

$$(\Delta)\gamma_{\mathrm{inel}}^N(y,Q_0^2)=0, \quad (1.2)$$

at $Q_0^2=0.26\,\mathrm{GeV}^2$, evolved for $Q^2>Q_0^2$ according to the leading order (LO) equation

$$\begin{aligned}&\frac{\mathrm{d}(\Delta)\gamma_{\mathrm{inel}}^N(y,Q^2)}{\mathrm{d}\ln Q^2}\\&=\frac{\alpha}{2\pi}\sum_{q=u,d,s}e_q^2\int_y^1\frac{\mathrm{d}x}{x}(\Delta)P_{\gamma q}\left(\frac{y}{x}\right)\\&\times\left[(\Delta)q^N(x,Q^2)+(\Delta)\bar{q}^N(x,Q^2)\right], \quad (1.3)\end{aligned}$$

with the unpolarized and polarized parton distributions in LO taken from [3,4].

As stated in [1], the boundary conditions (1.2) are not compelling but should be tested experimentally. However at large scales Q^2 the results become rather insensitive to details at the input scale Q_0^2 and thus the vanishing boundary conditions (1.2) yield reasonable results for $(\Delta)\gamma_{\mathrm{inel}}^N$ which are essentially determined by the quark and antiquark (sea) distributions of the nucleon in (1.3). At low scales Q^2, however, $(\Delta)\gamma_{\mathrm{inel}}^N(y,Q^2)$ depends obviously on the assumed details at the input scale Q_0^2. Such a situation is encountered at a fixed-target experiment, typically HERMES at DESY. At present it would be too speculative and arbitrary to study the effects due to a non-vanishing boundary $(\Delta)\gamma_{\mathrm{inel}}^N(y,Q_0^2)\neq 0$. Rather this should be examined experimentally if our expectations based on the vanishing boundary (1.2) turn out to be in disagreement with observations.

The photon distributions $(\Delta)\gamma^N$ of the nucleon, being the counterparts of the well-known photon distribution of the electron $\gamma^e(y,Q^2)$, are useful for cross section estimates in the equivalent photon approximation which simplifies more involved exact calculations (see [5], for example). Thus measurements of $(\Delta)\gamma^N(y,Q^2)$ are not only interesting on their own, but may provide additional information concerning $(\Delta)\overset{(-)}{q}{}^N$ in (1.3), in particular about the polarized parton distributions which are not well determined at present.

In the present paper we consider muon pair production $eN\to e\mu^+\mu^-X$ via the subprocess $\gamma^e\gamma^N\to\mu^+\mu^-$ and the Compton process $eN\to e\gamma X$ via the subprocess $e\gamma^N\to e\gamma$ for both the HERA collider experiments and the polarized and unpolarized fixed-target HERMES experiment at DESY. The Compton scattering process at HERA has already been studied in the equivalent photon approximation [6] as well as in an exact calculation [5]. It should be noted that a study of $NN\to\mu^+\mu^-X$ via $\gamma^N\gamma^N\to\mu^+\mu^-$ in hadron–hadron collisions is impossible [7,8] due to the dominance of the Drell–Yan subprocess $q^N\bar{q}^N\to\mu^+\mu^-$. The measurements at HERMES provide the unique opportunity of getting information concerning the *polarized* photon distributions, $\Delta\gamma^N$, of the nucleon as well.

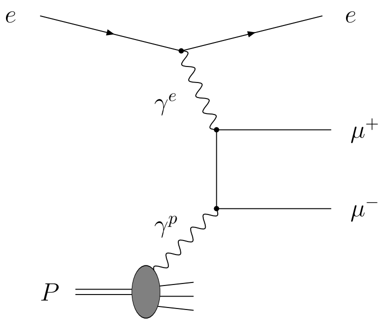

Fig. 1. Lowest order Feynman diagram for dimuon production in ep collisions. (The crossed $\hat{u}$-channel diagram is not shown)

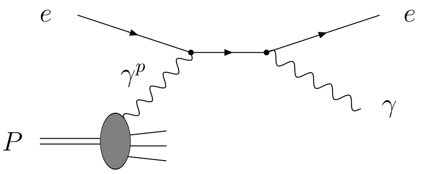

Fig. 2. Lowest order Feynman diagram for Compton scattering in ep collisions. (The crossed $\hat{u}$-channel contribution is not shown)

Our equivalent photon event rate estimates provide furthermore information concerning the possibility of measuring the polarized structure functions g_1^N via Compton scattering or dimuon production along the lines of [5] as extended to the spin dependent situation [9].

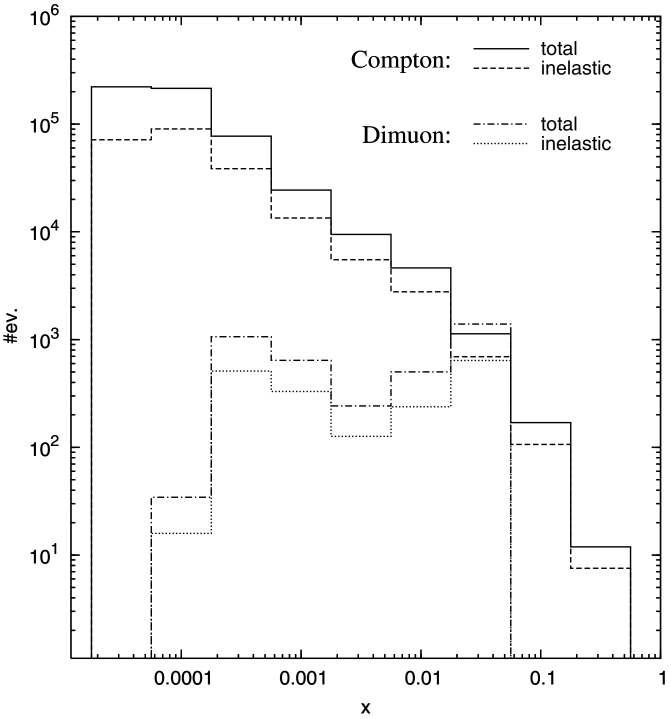

Fig. 3. Event rates for Compton ($e\gamma \to e\gamma$) and dimuon production ($\gamma\gamma \to \mu^+\mu^-$) processes at the HERA collider. The cuts applied are as described in the text

2 Theoretical framework

Considering first deep inelastic dimuon production $ep \to e\mu^+\mu^- X$ at HERA ($s = 4E_eE_p$) via the subprocess $\gamma^e\gamma^p \to \mu^+\mu^-$ as depicted in Fig. 1, let η_1 and η_2 be the (laboratory-frame) rapidities of μ^+ and μ^- measured along the proton beam direction. Then the production process can be written as[1]

$$\frac{\mathrm{d}\sigma}{\mathrm{d}\eta_1\mathrm{d}\eta_2\mathrm{d}\xi} = \frac{4\xi E_e^2}{1+\cosh(\eta_1-\eta_2)}\frac{\mathrm{e}^{\eta_1}+\mathrm{e}^{\eta_2}}{\mathrm{e}^{-\eta_1}+\mathrm{e}^{-\eta_2}} \times \xi\gamma^e(\xi,\hat{s})x\gamma^p(x,\hat{s})\frac{\mathrm{d}\hat{\sigma}}{\mathrm{d}\hat{t}}, \tag{2.1}$$

where $\hat{s} = (p_{\mu^+}+p_{\mu^-})^2$ denotes the dimuon invariant mass squared and the measured four-momenta p_{μ^+,μ^-} of the produced muons fix the momentum fractions either via

$$\xi = \frac{\sqrt{\hat{s}}}{2E_e}\left(\frac{\mathrm{e}^{-\eta_1}+\mathrm{e}^{-\eta_2}}{\mathrm{e}^{\eta_1}+\mathrm{e}^{\eta_2}}\right)^{1/2}, \tag{2.2}$$

$$x = \frac{\sqrt{\hat{s}}}{2E_p}\left(\frac{\mathrm{e}^{\eta_1}+\mathrm{e}^{\eta_2}}{\mathrm{e}^{-\eta_1}+\mathrm{e}^{-\eta_2}}\right)^{1/2}, \tag{2.3}$$

or equivalently via $xE_p+\xi E_e = p^0_{\mu^+}+p^0_{\mu^-}$ and $4\xi x E_eE_p = \hat{s}$ where $E_p = 820\,\mathrm{GeV}$, $E_e = 27.5\,\mathrm{GeV}$ are the colliding proton and electron energies. In the spirit of the leading order equivalent photon approximation underlying (2.1), we shall adopt the LO photon distribution $\gamma^p(x,\hat{s})$ of the proton in [1] as well as the LO equivalent photon distribution $\gamma^e(\xi,\hat{s})$ of the electron,

$$\gamma^e(\xi,\hat{s}) = \frac{\alpha}{2\pi}\frac{1+(1-\xi)^2}{\xi}\ln\frac{\hat{s}}{m_e^2}. \tag{2.4}$$

The cross section $\mathrm{d}\hat{\sigma}/\mathrm{d}\hat{t}$ in (2.1) for the subprocess $\gamma^e\gamma^p \to \mu^+\mu^-$ reads

$$\frac{\mathrm{d}\hat{\sigma}}{\mathrm{d}\hat{t}}^{\gamma\gamma\to\mu^+\mu^-} = \frac{2\pi\alpha^2}{\hat{s}^2}\left(\frac{\hat{t}}{\hat{u}}+\frac{\hat{u}}{\hat{t}}\right) = \frac{4\pi\alpha^2}{\hat{s}^2}\cosh(\eta_1-\eta_2)\,. \tag{2.5}$$

For the Compton process $ep \to e\gamma X$, proceeding via the subprocess $e\gamma^p \to e\gamma$ as depicted in Fig. 2, (2.1) is replaced by

$$\frac{\mathrm{d}\sigma}{\mathrm{d}\eta_e\mathrm{d}\eta_\gamma} = \frac{4E_e^2}{1+\cosh(\eta_e-\eta_\gamma)}\frac{\mathrm{e}^{\eta_e}+\mathrm{e}^{\eta_\gamma}}{\mathrm{e}^{-\eta_e}+\mathrm{e}^{-\eta_\gamma}}x\gamma^p(x,\hat{s})\frac{\mathrm{d}\hat{\sigma}}{\mathrm{d}\hat{t}}, \tag{2.6}$$

---

[1] A useful summary of the relevant kinematics can be found in Appendix D of [10] where the c.m. rapidities y_i have been used which are related to our laboratory-frame rapidities η_i via $y_i = \eta_i - \ln(E_p/E_e)^{1/2}$ for HERA (η_i is defined to be positive in the proton forward direction) and $y_i = \eta_i + \ln(M/2E_e)^{1/2}$ for HERMES (with η_i being positive in the electron forward direction). Notice that, besides η_1 and η_2, we have chosen ξ in (2.2) as third independent kinematical variable in (2.1) instead of the more commonly used $\hat{s}$ or the transverse momentum p_T of one of the two muons (which balance each other in LO), related by $\hat{s} = 2p_\mathrm{T}^2[1+\cosh(\eta_1-\eta_2)]$

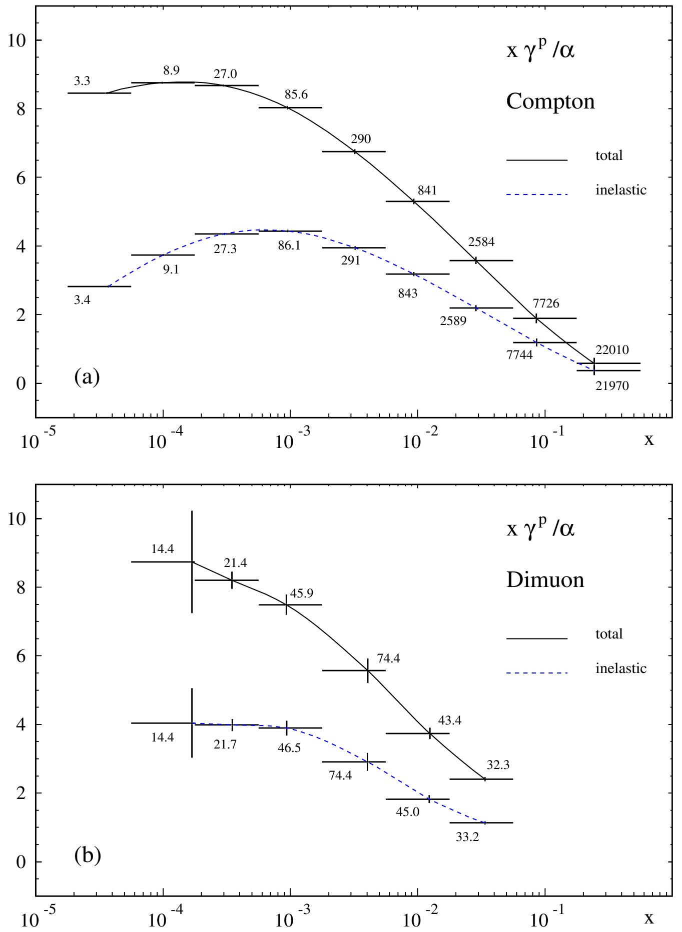

Fig. 4a,b. Expected statistical accuracy of the determination of $\gamma^p(\langle x\rangle, \langle\hat{s}\rangle)$ via **a** the Compton process and **b** the dimuon production process at the HERA collider. The numbers indicate the average scale $\langle\hat{s}\rangle$ (in GeV^2 units) for each x-bin

i.e., $\xi = 1$ and with $\eta_{e,\gamma}$ the rapidities of the produced (outgoing) electron and photon measured, again, in the proton beam direction. The cross section $\mathrm{d}\hat{\sigma}/\mathrm{d}\hat{t}$ for the subprocess $e\gamma^p \to e\gamma$ reads

$$\frac{\mathrm{d}\hat{\sigma}^{\,e\gamma\to e\gamma}}{\mathrm{d}\hat{t}} = -\frac{2\pi\alpha^2}{\hat{s}^2}\left(\frac{\hat{s}}{\hat{u}} + \frac{\hat{u}}{\hat{s}}\right), \qquad (2.7)$$

with $\hat{s} = (p_e + p_\gamma)^2$ and $-\hat{s}/\hat{u} = 1 + \mathrm{e}^{\eta_e - \eta_\gamma}$. Here x is fixed by (2.3) or by either $E_e + xE_p = p_e^0 + p_\gamma^0$ or $4xE_eE_p = \hat{s}$.

The extension to the fixed-target experiment HERMES ($s = 2ME_e$) is obtained via $E_p \to M/2$ and $\eta_i \to -\eta_i$ everywhere with η_i now corresponding to the rapidities of the observed particles with respect to the electron beam direction. Furthermore, at HERMES one may study also $\gamma^n(x, \hat{s})$ as well as the polarized $\Delta\gamma^N(x, \hat{s})$ in [1] by utilizing

$$\Delta\gamma^e(\xi, \hat{s}) = \frac{\alpha}{2\pi}\frac{1-(1-\xi)^2}{\xi}\ln\frac{\hat{s}}{m_e^2}, \qquad (2.8)$$

in the obvious spin dependent counterpart of (2.1), while the relevant LO cross sections for the polarized subprocesses are given by

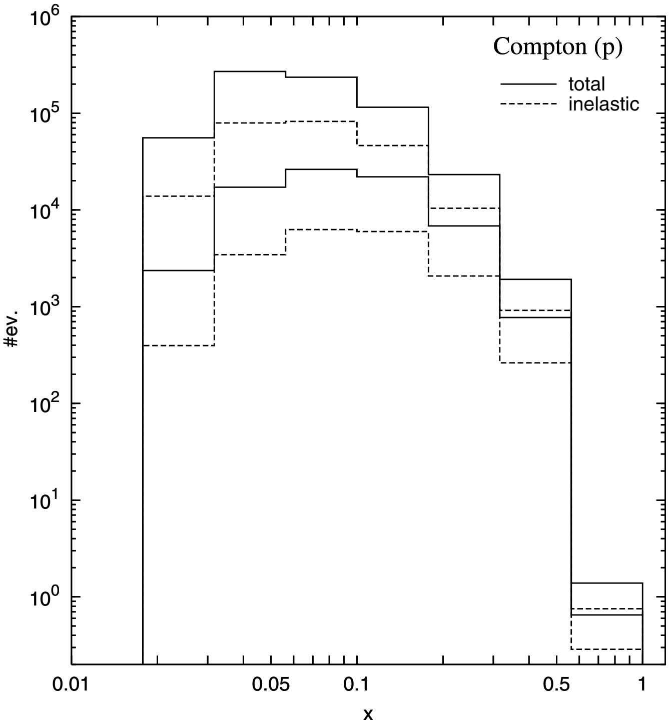

Fig. 5. Event rates for the Compton process at HERMES using an (un)polarized proton target. The upper (solid and dashed) curves refer to an unpolarized proton, whereas the lower ones refer to a polarized proton target. The cuts applied are as described in the text

$$\frac{\mathrm{d}\Delta\hat{\sigma}^{\,\gamma\gamma\to\mu^+\mu^-}}{\mathrm{d}\hat{t}} = -\frac{\mathrm{d}\hat{\sigma}^{\,\gamma\gamma\to\mu^+\mu^-}}{\mathrm{d}\hat{t}}, \qquad (2.9)$$

$$\frac{\mathrm{d}\Delta\hat{\sigma}^{\,e\gamma\to e\gamma}}{\mathrm{d}\hat{t}} = -\frac{2\pi\alpha^2}{\hat{s}^2}\left(\frac{\hat{s}}{\hat{u}} - \frac{\hat{u}}{\hat{s}}\right), \qquad (2.10)$$

with $-\hat{s}/\hat{u} = 1 + \mathrm{e}^{\eta_\gamma - \eta_e}$. These expressions apply obviously also to the COMPASS μp experiment at CERN whose higher incoming lepton energies ($E_\mu = 50$–$200\,\mathrm{GeV}$) enable the determination of $\Delta\gamma^N(x, Q^2)$ at lower values of x as compared to the corresponding measurements at HERMES. (Notice that for a muon beam one has obviously to replace m_e by m_μ in (2.4) and (2.8).)

3 Results

We shall present here the expected number of events for the accessible x-bins at HERA collider experiments and at the fixed-target HERMES experiment subject to some representative kinematical cuts which, of course, may be slightly modified in the actual experiments. These cuts entail $\hat{s} \geq \hat{s}_{\min}$, $\eta_{\min} \leq \eta_i \leq \eta_{\max}$ and $E_i \geq E_{\min}$, where E_i are the energies of the observed outgoing particles. The relevant integration ranges at HERA are fixed via $0 \leq \xi \leq 1$, $\hat{s}_{\min}/4\xi E_eE_p \leq x \leq 1$ with $\hat{s}$ given by $\hat{s} = 4x\xi E_eE_p$ while η_i are constrained by $\eta_1 + \eta_2 = \ln((xE_p)/(\xi E_e))$

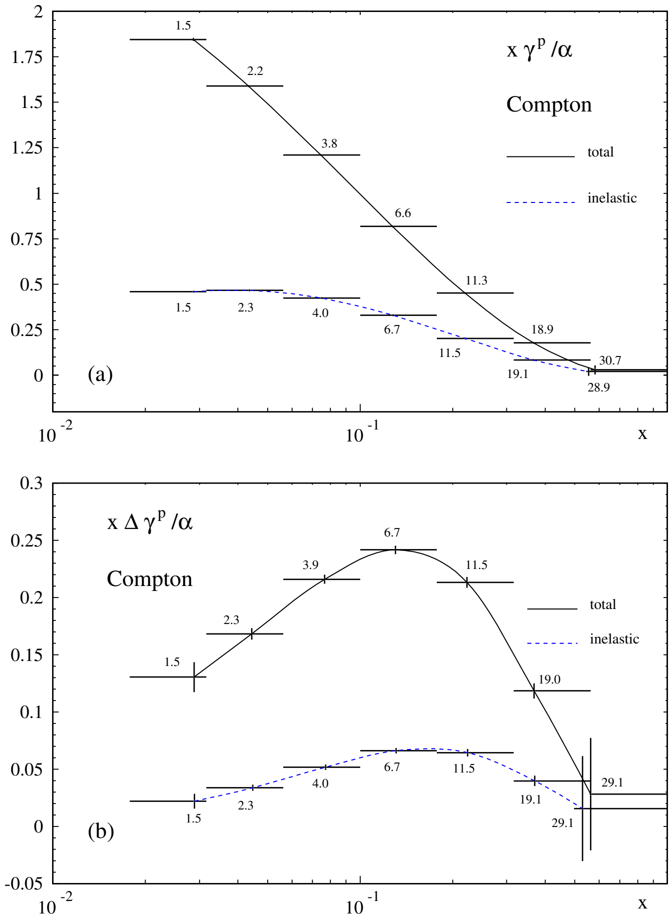

Fig. 6a,b. Expected statistical accuracy of the determination of **a** $\gamma^p(\langle x\rangle, \langle\hat{s}\rangle)$ and **b** $\Delta\gamma^p(\langle x\rangle, \langle\hat{s}\rangle)$ via the Compton process at HERMES using an (un)polarized proton target. The numbers indicate the average scale $\langle\hat{s}\rangle$ (in GeV^2 units) for each bin

which follows from (2.3). Here $\xi = 1$, $\eta_1 = \eta_\gamma$, $\eta_2 = \eta_e$ for the Compton scattering process, (2.6). The relation $\eta_i - \eta_j = \ln\left[(\xi E_e/E_i)(1 + \mathrm{e}^{2\eta_i}) - 1\right]$ as obtained from the outgoing particle energy E_i and its transverse momentum [10] further restricts the integration range of $\eta_{i,j}$ as dictated by $E_i \geq (E_i)_{\mathrm{min}}$. At HERMES $E_p \to M/2$ and $\eta_i \to -\eta_i$ in the above expressions with η_i the outgoing particle rapidity with respect to the ingoing lepton direction.

In the following we shall consider $E_{\mathrm{min}} = 4\,\mathrm{GeV}$. For the Compton scattering process we further employ $\hat{s}_{\mathrm{min}} = 1\,\mathrm{GeV}^2$ so as to guarantee the applicability of perturbative QCD, i.e., the relevance of the utilized [1] $(\Delta)\gamma^N(x, \hat{s})$. For the dimuon production process we shall impose $\hat{s}_{\mathrm{min}} = M^2[\Psi(2S)] = (3.7\,\mathrm{GeV})^2$ so as to evade the dimuon background induced by charmonium decays at HERMES (higher charmonium states have negligible branching ratios into dimuons); for HERA we impose in addition $\hat{s}_{\mathrm{max}} = M^2[\Upsilon(1S)] = (9.4\,\mathrm{GeV})^2$ in order to avoid the dimuon events induced by bottomium decays. Finally, at HERA we consider $\eta_{\mathrm{min}} = -3.8$, $\eta_{\mathrm{max}} = 3.8$ and at HER-

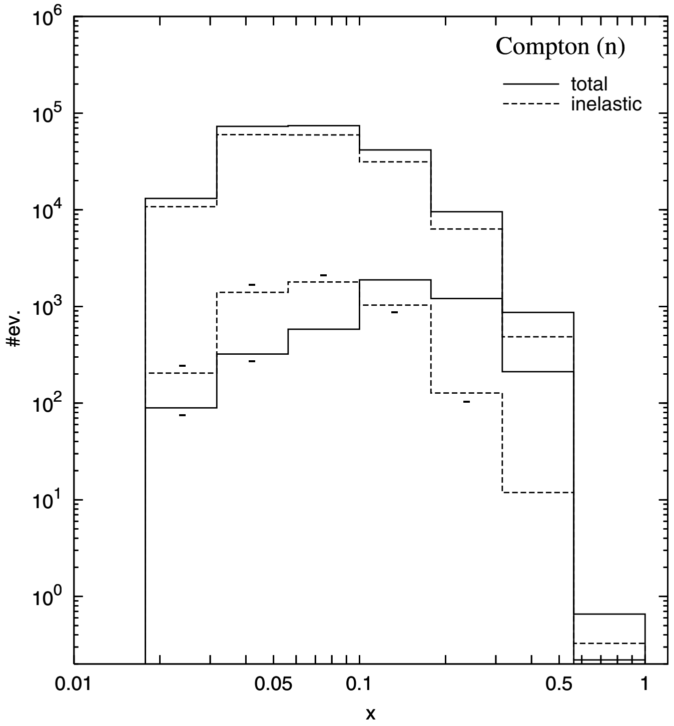

Fig. 7. As in Fig. 5, but for a neutron target. The negative signs at some lower-x-bins indicate that the polarized total cross section and/or inelastic contribution is negative

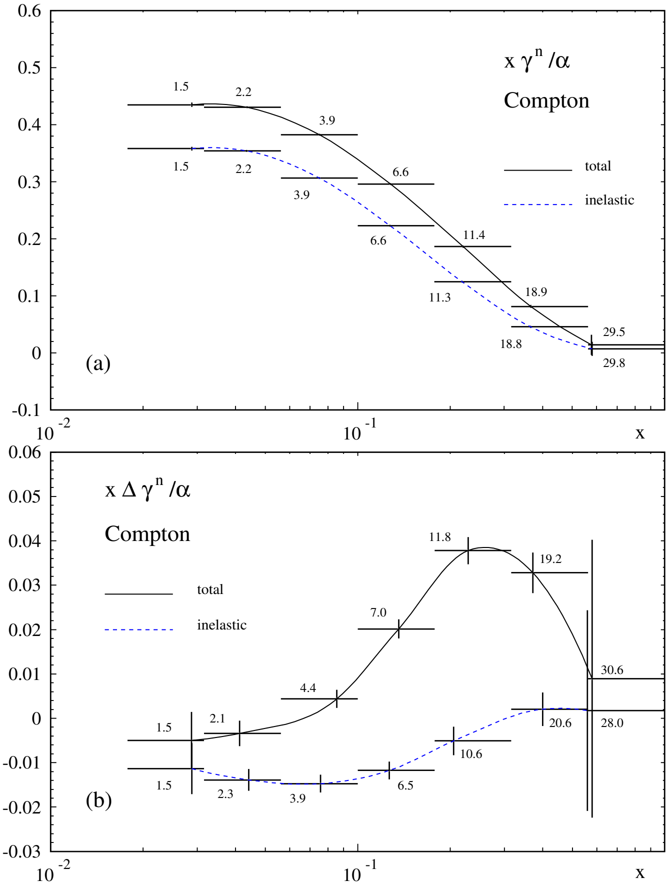

Fig. 8a,b. As in Fig. 6, but for a neutron target

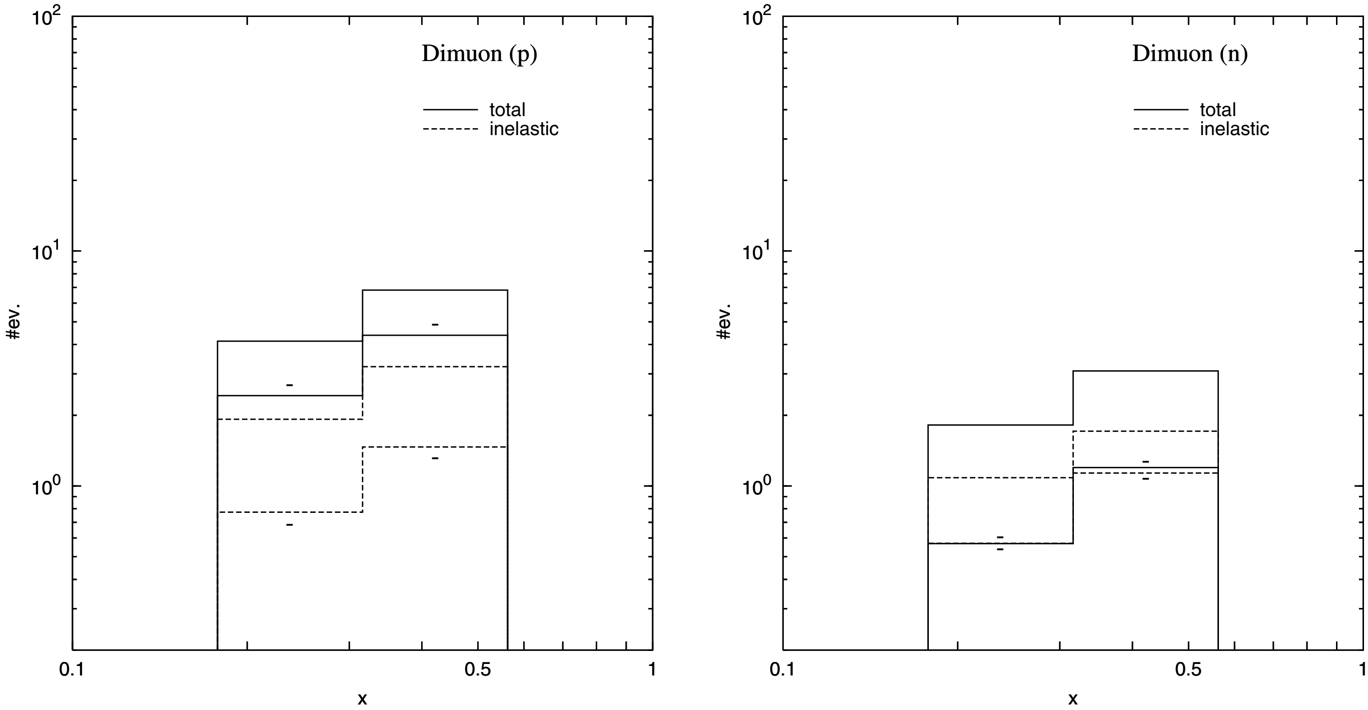

Fig. 9. As in Fig. 5, but for dimuon production at HERMES using (un)polarized proton and neutron targets. The lower solid and dashed curves refer to a polarized nucleon target and the negative signs indicate that the polarized cross sections are negative

MES $\eta_{\min} = 2.3$, $\eta_{\max} = 3.9$. The integrated luminosities considered are $\mathcal{L}_{\text{HERA}} = 100\,\text{pb}^{-1}$ and $\mathcal{L}_{\text{HERMES}} = 1\,\text{fb}^{-1}$.

In Fig. 3 the histograms depict the expected number of dimuon and Compton events at HERA found by integrating (2.1) and (2.6) applying the aforementioned cuts and constraints. The important inelastic contribution due to γ^p_{inel} in (1.1), being calculated according to (1.3) using the minimal boundary condition (1.2), is shown separately by the dashed curves. To illustrate the experimental extraction of $\gamma^p(x, \hat{s})$ we translate the information in Fig. 3 into a statement on the accuracy of a possible measurement by evaluating $\gamma^p(\langle x\rangle, \langle\hat{s}\rangle)$ at the averages $\langle x\rangle$, $\langle\hat{s}\rangle$ determined from the event sample in Fig. 3. Assuming that in each bin the error is only statistical, i.e. $\delta\gamma = \pm\gamma/N_{\text{bin}}^{1/2}$, the results for $x\gamma/\alpha$ are shown in Fig. 4. It should be noticed that the statistical accuracy shown will increase if $\gamma^p_{\text{inel}}(x, Q_0^2) \neq 0$ in contrast to our vanishing boundary condition (1.2) used in all our present calculations. Our results for the Compton process in Figs. 4 and 5 are, apart from our somewhat different cut requirements, similar to the ones presented in [6].

Apart from testing $\gamma^N(x, \hat{s})$ at larger values of x, the fixed-target HERMES experiment can measure the polarized $\Delta\gamma^N(x, \hat{s})$ as well. In Fig. 5 we show the expected number of Compton events for an (un)polarized proton target. The accuracy of a possible measurement of $\gamma^p(\langle x\rangle, \langle\hat{s}\rangle)$ and $\Delta\gamma^p(\langle x\rangle, \langle\hat{s}\rangle)$ is illustrated in Fig. 6 where the averages $\langle x\rangle$, $\langle\hat{s}\rangle$ are determined from the event sample in Fig. 5 by assuming that the error is only statistical also for the polarized photon distribution, i.e. $\delta(\Delta\gamma) = \pm(N_{\text{bin}}^{1/2}/|\Delta N_{\text{bin}}|)\Delta\gamma$. The analogous expectations for an (un)polarized neutron target are shown in Figs. 7 and 8. It should be pointed out that, according to Figs. 6b and 8b, HERMES measurements will be sufficiently accurate to delineate even the polarized $\Delta\gamma^{p,n}$ distributions in the medium- to small-x region, in particular the theoretically more speculative inelastic contributions.

For completeness, in Figs. 9 and 10 we also show the results for dimuon production at HERMES for (un)polarized proton and neutron targets despite the fact that the statistics will be far inferior to the Compton process.

The dimuon production can obviously proceed also via the genuine Drell–Yan subprocess $q\bar{q} \to \mu^+\mu^-$ where one of the (anti)quarks resides in the resolved component of the photon emitted by the electron. However, as already noted in [11], this contribution is negligible as compared to the one due to the Bethe–Heitler subprocess $\gamma\gamma \to \mu^+\mu^-$. The unpolarized dimuon production rates at HERA where also studied in [11,12] utilizing, however, different prescriptions for the photon content of the nucleon.
Exact expressions for the Bethe–Heitler contribution to the longitudinally polarized $\gamma N \to \mu^+\mu^- X$ process are presented in [13] but no estimates for the expected production rates at, say, HERMES or COMPASS are given.

4 Summary

The analysis of the production rates of lepton–photon and muon pairs at the colliding beam experiments at HERA and the fixed-target HERMES facility, as evaluated in the

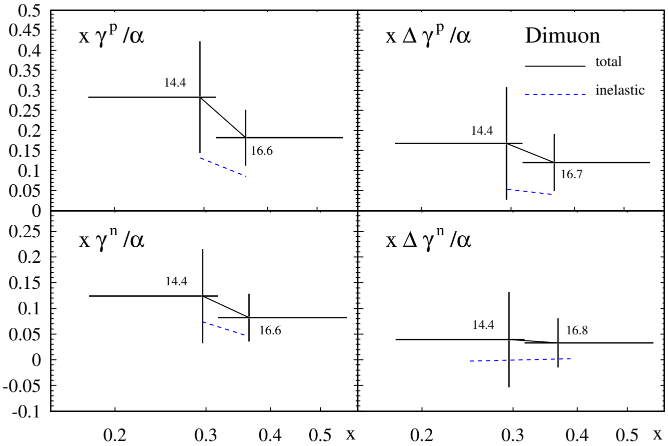

Fig. 10. As in Fig. 6, but for dimuon production at HERMES for (un)polarized proton and neutron targets. The statistical accuracy for the inelastic contributions is similar to those shown for the total result, except for the almost vanishing $\Delta\gamma^n_{\rm inel}$

leading order equivalent photon approximation, demonstrates the feasibility of determining the polarized and unpolarized equivalent photon distributions of the nucleon in the available kinematical regions. The above mentioned production rates can obviously be determined in a more accurate calculation along the lines of [5], involving the polarized and unpolarized structure functions $g^N_{1,2}$ and $F^N_{1,2}$, respectively, of the nucleon. The expected production rates are similar to those obtained in our equivalent photon approximation (cf. Figures 5.7 and 5.12 of [14]). It thus turns out that lepton–photon and muon pair production at HERA and HERMES may provide an additional and independent source of information concerning these structure functions.

Acknowledgements. This work has been supported in part by the Bundesministerium für Bildung und Forschung, Berlin/Bonn.

References

1. M. Glück, C. Pisano, E. Reya, Phys. Lett. B **540**, 75 (2002), and references therein
2. B.A. Kniehl, Phys. Lett. B **254**, 267 (1991)
3. M. Glück, E. Reya, A. Vogt, Eur. Phys. J. C **5**, 461 (1998)
4. M. Glück, E. Reya, M. Stratmann, W. Vogelsang, Phys. Rev. D **63**, 094005 (2001)
5. A. Courau, P. Kessler, Phys. Rev. D **46**, 117 (1992)
6. A. De Rújula, W. Vogelsang, Phys. Lett. B **451**, 437 (1999)
7. M. Drees, R.M. Godbole, M. Nowakowski, S.D. Rindani, Phys. Rev. D **50**, 2335 (1994)
8. J. Ohnemus, T.F. Walsh, P.M. Zerwas, Phys. Lett. B **328**, 369 (1994)
9. Work in progress
10. G. Sterman et al., CTEQ Collaboration, Rev. Mod. Phys. **67**, 157 (1995)
11. N. Arteaga-Romero, C. Carimalo, P. Kessler, Z. Phys. C **52**, 289 (1991)
12. P.J. Bussey, B. Levtchenko, A. Shumilin, hep-ph/9609273
13. T. Gehrmann, M. Stratmann, Phys. Rev. D **56**, 5839 (1997)
14. V. Lendermann, H1 Collaboration, DESY-THESIS-2002-004